Diffraction in crystalline colloidal-array photonic crystals

Sanford A. Asher,* Jesse M. Weissman, Alexander Tikhonov, Rob D. Coalson, and Rasu Kesavamoorthy†
Department of Chemistry, University of Pittsburgh, Pittsburgh, Pennsylvania 15260, USA
(Received 15 September 2003; published 23 June 2004)

We characterized the diffraction and crystal structure of a crystalline colloidal array (CCA) photonic crystal composed of 270 nm diameter polystyrene spheres which have a nearest neighbor spacing of ~540 nm. This CCA diffracts light in first order at ≈1200 nm and shows strong diffraction in the visible spectral region from higher order planes. We quantitatively examined the relative diffraction intensities of the putative fcc (111), (200), (220), and (311) planes. Comparing these intensities to those calculated theoretically we find that the crystal structure is fcc with significant stacking faults. Essentially, no light transmits at the Bragg angle for the fcc (111) planes even through thin ~40 μm thick CCA. However, much of this light is diffusely scattered about the Bragg angle due to crystal imperfections. Significant transmission occurs from thin samples oriented at the Bragg condition for the fcc (200), (220), and (311) planes. We also observe moderately intense two-dimensional diffraction from the first few layers at the crystal surfaces. We also examined the sample thickness dependence of diffraction from CCA photonic crystals prepared from ~120 nm polystyrene spheres whose fcc (111) planes diffract in the visible spectral region. These experimental observations, aided by calculations based upon a simple but flexible model of light scattering from an arbitrary collection of colloidal spheres, make clear that fabrication of three-dimensional photonic band gap crystals will be challenged by crystal imperfections.

DOI: 10.1103/PhysRevE.69.066619 PACS number(s): 42.25.Dd, 82.70.Dd, 78.67.−n, 61.72.Nn

I. INTRODUCTION

The recent intense interest in the design and fabrication of photonic band gap crystals (PBGC) stems from the unusual phenomena that these materials potentially display [1–13]. A full three-dimensional PBGC would not possess eigenmodes for the propagation of electromagnetic radiation within a defined spectral interval. Thus, light within this interval could not propagate in the material. These materials would not support spontaneous emission events such as fluorescence. PBGC materials could significantly impact areas of optoelectronics, laser design, and telecommunications.

PBGC consist of periodic dielectric structures, which are designed to create an optical band gap. The earliest PBGC demonstrated were in the microwave region where periodic structures were machined [8]. The structures required to achieve full three-dimensional band gaps have been theoretically well described [1–6]. For example, in the visible spectral region a PBGC could be fabricated by creating a periodic structure of interpenetrating face centered cubic lattices similar to that of diamond [1,4,5]. The basis of the lattice would be spheres of high refractive index and the region between spheres would be filled with a medium of sufficiently lower refractive index, that the refractive index ratio [4] would exceed ~2.8. In addition, theoretical calculations suggest that PBGC could be fabricated by utilizing more complex periodic structures [3].

Although the theoretical understanding of PBGC materials has become relatively mature, as yet there is no material fabricated, as far as we know, that has been shown to possess a complete band gap in the visible or near-IR spectral regions. Some previous attempts to fabricate systems that slightly approximate PBGC in the visible spectral region have utilized inverse opal structures, where close packed polymer sphere arrays were formed. High refractive index materials were then incorporated in the interstices [14–16]. The close packed polymer spheres were then vaporized to form an air sphere lattice with a high refractive index contrast. These structures were not expected to show three-dimensional band gaps; they showed one-dimensional band gaps similar to those previously observed for crystalline colloidal array (CCA) photonic crystals [17–30].

There is an extensive literature which has explored the diffraction properties of photonic crystals prepared through the use of crystalline colloidal self-assembly [11,17–37]. CCAs form when highly charged, monodisperse colloidal particles dispersed in very low ionic strength aqueous media crystallize into cubic array structures. The strong electrostatic interactions between the particles force the colloid to minimize the total system energy by arranging into either a face-centered cubic (fcc) or body-centered cubic (bcc) crystalline array, depending on the particle number density and the strength of the repulsive interactions [19,20,37]. CCA lattice constants are typically on the order of hundreds of nanometers, so the arrays diffract near-UV, visible, and near-IR light. CCA appear brightly colored and opalescent because of the diffraction of visible light. Our group was the first to demonstrate the formation of photonic crystals from CCA [20,22–24] and we have used these materials to fabricate optical notch filters [20–24], optical switches [25,26] and photonic crystal chemical sensors [27,28].

CCA photonic crystals diffract light very efficiently; thin films <50 μm thick attenuate essentially all of the light within the one-dimensional band gap [20]. Recently, we be-

*Author to whom correspondence should be addressed. FAX: 412-624-0588; Email address: asher@pitt.edu
†Also at Materials Science Division, Indira Gandhi Centre for Atomic Research, Kalpakkam 603102, India.

gan to study CCA with large periodicities, which diffract light in the near-IR spectral region. These photonic crystals not only diffract IR light in first order, but also diffract light in the visible wavelength region in higher order [29]. Visible and UV wavelength light is also diffracted by higher Miller index CCA crystal planes [29]. Experimentally, we find that these CCA crystals do not appear to transmit visible light at any propagation angle. This is certainly not because this CCA is a three-dimensional (3D) PBGC, since the refractive index ratio between the polystyrene ($n=1.6$) and the water medium (1.336) is small and a noninverted fcc structure cannot form a 3D PBGC [4–6].

In the work here we have thoroughly characterized the crystal structure of this near-IR diffracting CCA, and examined its transmission and diffraction. We also examined the dependence of diffraction on the particle number density and sample thickness. As we found earlier [20], a significant amount of the incident light is diffusely scattered at angles close to the diffraction angles. This diffuse scattering results from crystal imperfections. Aided by computations based on a simple yet effective model of light scattering from an arbitrary collection of colloidal spheres, we discuss the role of defects on the optical performance of CCA photonic crystals and challenge the theoretical community to develop further refined models that incorporate less than perfect crystal structures [30–33]. These models will certainly be necessary to understand the optical properties of the inevitably less than perfect, highly defective PBGC which will be fabricated in the nearest future.

II. EXPERIMENT

A. Materials

Highly charged polystyrene colloidal particles with diameters of 118, 119, and 270 nm and $<2\%$ polydispersity were prepared by emulsion polymerization as described elsewhere [34]. The colloids were cleaned by repeated dialysis against ultrapure water and then shaken with mixed bed ion exchange resin. Particle sizes were measured by quasielastic light scattering and by transmission electron microscopy. Particle surface charge was measured by titration against NaOH to have values of 6600, 7200, and 79 000 charges per particle for the 118, 119, and 270 nm diameter colloids, respectively. The relative standard deviations in measured charge were estimated to be less than 5%.

CCA that diffracted visible wavelength light in first order at normal incidence (visible CCA) were prepared from the 118 and 119 nm diameter polystyrene colloids, diluted to $\sim 5-10\,\%$ volume fractions in ultrapure water. The CCA that diffracted near-IR light (IR CCA) were made by diluting the 270 nm diameter colloids to give an $\sim 8\%$ volume fraction. All of the CCA crystals were prepared within cells which consisted of two quartz disks separated by thin spacers. One disk had two injection ports drilled into it, through which the CCA solution was injected. We utilized 25 μm Teflon spacers, 40 μm polyethylene spacers, and 125 μm and 250 μm parafilm spacers. The surfaces of the quartz plates were coated with a hydrophobic polysiloxane (Sigmacote, Sigma), which allowed for even flow of the CCA into the thin cells.

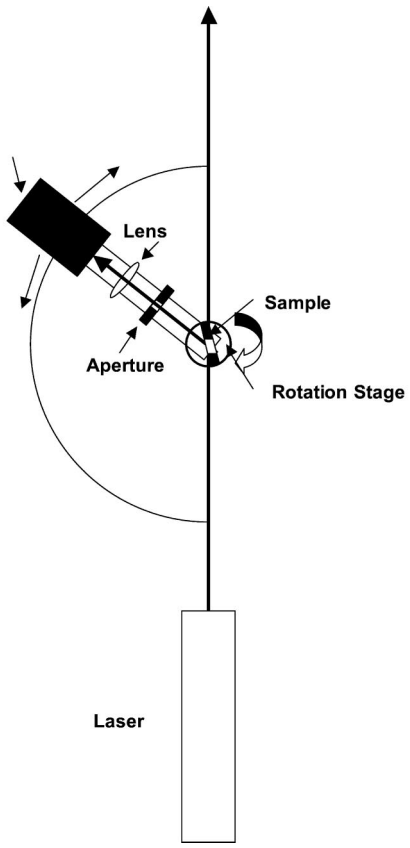

FIG. 1. The visible wavelength CCA diffraction measurements utilized a sample mounted on a rotation stage with an adjustable aperture detector mounted on a rotating arm.

B. Transmission measurements

Transmission measurements were performed by using a Perkin-Elmer λ-9 UV/visible/near-IR spectrophotometer. The CCA crystals in their cells were mounted on a rotation stage, in order to measure transmission as a function of angle. For some measurements the incident light was polarized with a calcite polarizer mounted in the sample beam path.

C. Diffraction measurements of visible CCA

Optical diffraction measurements for the visible CCA were made by using the 457 and 488 nm beams from an argon-ion laser (Spectra Physics). The experimental setup is shown in Fig. 1. The CCA samples were mounted on a rotation stage. Transmitted and diffracted intensities were measured with an energy probe detector (laser probe). An adjustable aperture was mounted on the detector arm between the sample and detector. The aperture diameter was switched between ~ 1.0 mm, to collect only the specularly diffracted laser beam, and ~ 9.0 mm to collect a scattering angle of $\sim 5.0°$.

Transmission and diffraction measurements were made according to the following procedure. The CCA sample was mounted on a rotation stage with the cell plane normal to the laser beam. The CCA sample was then rotated both about the vertical axis and the sample plane normal until it met the

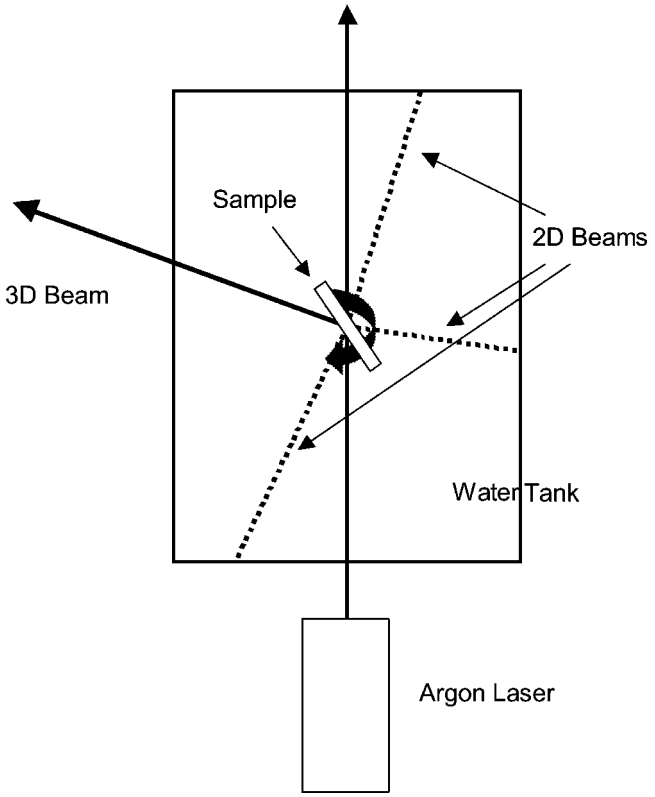

FIG. 2. Experimental setup for diffraction measurements from IR CCA. The sample was suspended in a tank of water to minimize reflections and to avoid correcting the scattered light angles for refraction.

diffraction condition, which was identified by the transmitted intensity minimum. Transmitted intensities were then measured for both aperture diameters. The diffracted intensities were measured by moving the detector arm to the appropriate diffracted beam angles.

Diffraction bandwidth measurements of the visible CCA were performed using a $\theta-2\theta$ scan. The sample was rotated in 1.0° increments around the maximum diffraction angle, and the detector arm was correspondingly rotated in 2.0° increments, while recording the intensity of the sum of the diffracted and reflected light.

D. Diffraction measurements of IR CCA

The cell containing the CCA was suspended from a rotation stage in the center of a rectangular tank filled with water (Fig. 2). The CCA cell could also be independently rotated about the cell normal. Diffracted light from the CCA was imaged onto paper screens attached to the exterior of the tank walls. The diffraction angles were determined geometrically.

Diffraction intensities were usually measured with the IR CCA cell in the water tank. The diffracted beam was allowed to transmit through the walls of the tank and the diffracted beam (angular width $\sim 1.5\times 10^{-4}$ steradians) exiting the tank was collected and focused onto an energy probe to record its intensity. The intensity was corrected for reflection at the air/glass interface.

The angular diffraction bandwidths for the IR CCA were measured using a different procedure than for the visible CCA. We measured relative intensities by placing an energy probe detector flush against the paper screen on the exterior of the water tank at a position corresponding to the maximum diffracted intensity. With the detector location fixed, the CCA was rotated about the Bragg angle while the diffracted intensity was recorded.

E. Kossel ring measurements

The CCA samples were placed in a water tank as described above. The Kossel ring patterns [19,20,35] observed on the paper screens were photographed by a charge-coupled device (CCD) camera. The Kossel ring patterns were calculated with a program written using MATHCAD.

III. RESULTS AND DISCUSSION

A. Determination of crystal structure and orientation

We carefully examined the diffraction patterns to determine the crystal structure and orientation. The crystal structure was determined from the measured diffraction angles and from the IR CCA Kossel ring patterns [19,20,35]; the large lattice constant of the IR CCA allows studies of diffraction in the visible spectral region from higher Miller index lattice planes.

We determined the longest plane spacings by measuring extinction of the CCA sample at normal incidence (Fig. 3). A strong symmetric extinction peak occurs at ~1200 nm. The CCA is transmittive down to ~700 nm, below which numerous strong extinction features occur. The ~1200 nm extinction peak blue-shifts approximately follow Bragg's law as the CCA sample is rotated off of normal incidence.

CCA are reported to form fcc or bcc crystal structures [19,20,37]. We examined this CCA sample to determine whether it was fcc or bcc by testing it for Bragg diffraction from higher order fcc and bcc planes. If the crystal were fcc, then the ~1200 nm diffraction must derive from the (111) planes. The spacing of any set of fcc planes (*hkl*) is related [19] to the crystal lattice constant a by

$$d_{hkl} = \frac{a}{\sqrt{h^2 + k^2 + l^2}},$$

where h, k, and l are the crystal plane Miller indices. From the ~1200 nm diffraction peak, we obtain an fcc lattice constant $a = 766$ nm using Bragg's Law

$$\lambda_0 = 2 n_c d_{hkl} \sin(\theta_b),$$

where λ_0 is the wavelength in vacuum of the diffracted light, n_c is the refractive index of the crystal ($n_c = 1.359$) [19,20], d is the spacing of the lattice planes of interest, and θ_b is the Bragg glancing angle (90° here). The angle between any two fcc crystal planes is

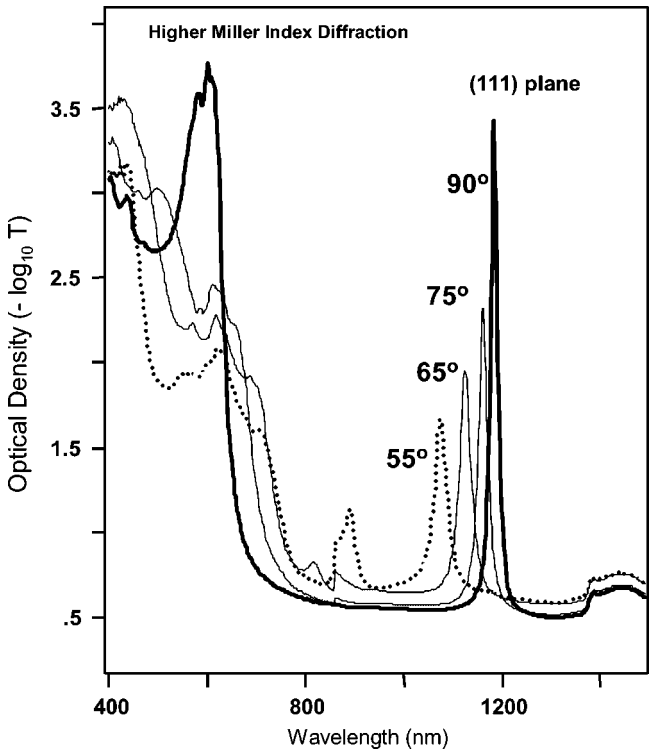

FIG. 3. Extinction spectra of CCA measured by using a UV-visible-near-IR spectrophotometer as a function of incident angles. The ~1200 nm peak is from the fcc (111) planes. The diffraction blue shifts as the sample is rotated. The large peak at ~600 nm at normal incidence derives from a superposition of (200), (220), (311), and (222) diffraction peaks [29]. The peaks no longer overlap when the sample is rotated off of normal incidence.

$$\cos\,\alpha = \frac{h_1h_2 + k_1k_2 + l_1l_2}{\sqrt{(h_1^2 + k_1^2 + l_1^2)\cdot(h_2^2 + k_2^2 + l_2^2)}}.$$

Thus, if the incident beam is normal to the (111) plane of an fcc CCA, diffraction from the (*hkl*) will be observed if the crystal is rotated by angle β,

$$\beta = \alpha \pm (90° - \theta_b),$$

and then the CCA is rotated about the normal to the (111) plane to search for diffraction of the (*hkl*) planes.

Table I lists the diffracting fcc crystal planes, their interplanar spacings, and the calculated and measured Bragg scattering angles for 488 nm incident beam for 40 μm and 125 μm thick CCA samples. The observed values of θ_b agree well with those calculated from Bragg's law. The rotation angles for the (200), (220), and (311) planes are 7.0°, 12.7°, and 8.8°, respectively. Because of the similar diffraction angles of the (222) [i.e., 2nd (111)] and (311) planes (54.4° and 51.3°, respectively) and their angular bandwidths, we observed overlapping diffraction from both planes at angles intermediate between the two Bragg angles.

To ensure that the CCA did not contain bcc or hexagonally close-packed (hcp) crystals, we looked for diffraction from the higher order bcc and hcp diffracting planes where we assumed that the ~1200 nm diffraction peak occurred from the (110) bcc planes or the (100) or (002) hcp planes. We found no diffraction for the bcc or hcp planes. Thus, we conclude that the IR CCA are, on average, fcc crystals, with no evidence of bcc or hcp crystallites.

TABLE I. Comparison of predicted and measured Bragg diffraction and scattering angles for each set of fcc lattice planes of the IR CCA. The measured values are estimated to be accurate to ±1°.

Plane	d (nm)	θ_b (Calculated)	θ_b (Measured) 40 μm	θ_b (Measured) 125 μm
(111)	442.2	24.0	22.7	23.8
2nd (111)	221.1	54.4	53.0	55.0
(200)	383	28.0	27.4	27.8
(220)	270.8	41.7	42.0	43.1
(311)	230.9	51.3	52.0	53.0
$(\bar{1}11)$	442.2	24.0	24.3	24.1
$(\bar{1}\bar{1}\bar{1})$	442.2	24.0	23.8	24.7

In addition to confirming diffraction from these higher Miller index fcc planes, we also measured the angular relationships between these planes by first rotating the sample to the appropriate angle for Bragg diffraction from one set of planes and then performing a second rotation around the axis normal to the putative (111) planes which are parallel to the quartz plates. We expect C_3 symmetry for diffraction from the (200), (220), and (311) planes upon rotation about the [111] direction. In contrast, we observe C_6 symmetry, where diffraction occurs every 60°. The angular orientation of this diffraction is identical to the hexagonal set of the 2D diffraction beams, as discussed below. This indicates the presence of stacking faults which rotate the diffraction angle by 60° about the (111) plane normal.

We also observed two-dimensional diffraction from the first few crystal planes of the IR CCA, in addition to the 3D diffraction. The hexagonally ordered (111) planes, which align parallel to the cell walls give rise to a hexagonal set of diffraction spots (Fig. 4). In contrast to 3D diffraction for a set of planes, which occurs for a single wavelength only for an incident angle that fulfills the Bragg condition, diffraction from a 2D hexagonal array occurs at all incident angles. The 2D diffraction condition is [17]

$$\sin\,\theta_1 + \sin\,\theta_2 = \frac{2\lambda_0}{\sqrt{3}n_cD},$$

where θ_1 is the angle of incidence, θ_2 is the diffraction angle n_c is the system refractive index, and D is the nearest neighbor particle spacing within the plane. For the case where the 2D diffraction comes from the (111) plane of an fcc lattice, $D = a/\sqrt{2}$.

We measured the 2D diffraction pattern in the water tank. The CCA cell was oriented with the line between filling holes along the axis of rotation. We translated the sample through the beam and observed that the 2D hexagonal pattern was identically oriented over the entire sample. Thus, the orientation of the hexagonal sphere packing within the planes is constant over the entire sample except for stacking

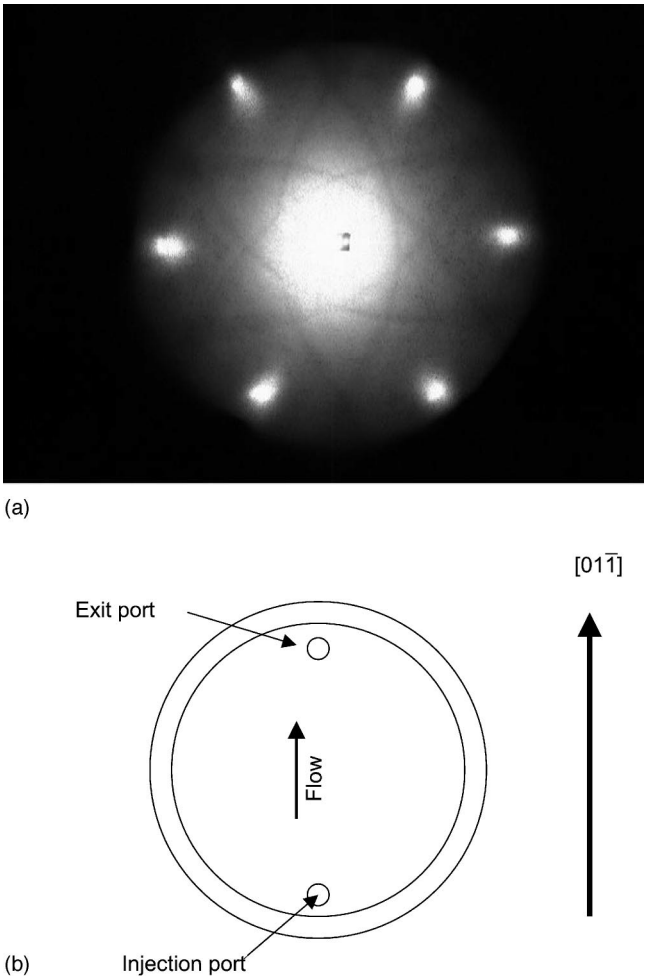

FIG. 4. (a) Photograph showing 2D diffraction spots from an IR CCA. A 457.9 nm laser beam is incident though a hole in the center of a paper screen outside a water tank containing the CCA oriented with its (111) planes normal to the beam. The hexagonal pattern of spots are created by 2D diffraction from the particles within the first few layers of the CCA. The star shaped pattern of lines are from Kossel rings (see below). (b) Diagram of cell used to contain CCA samples. The colloid solution was injected and flowed from one injection port out the other. Shear forces along the flow direction align the CCA.

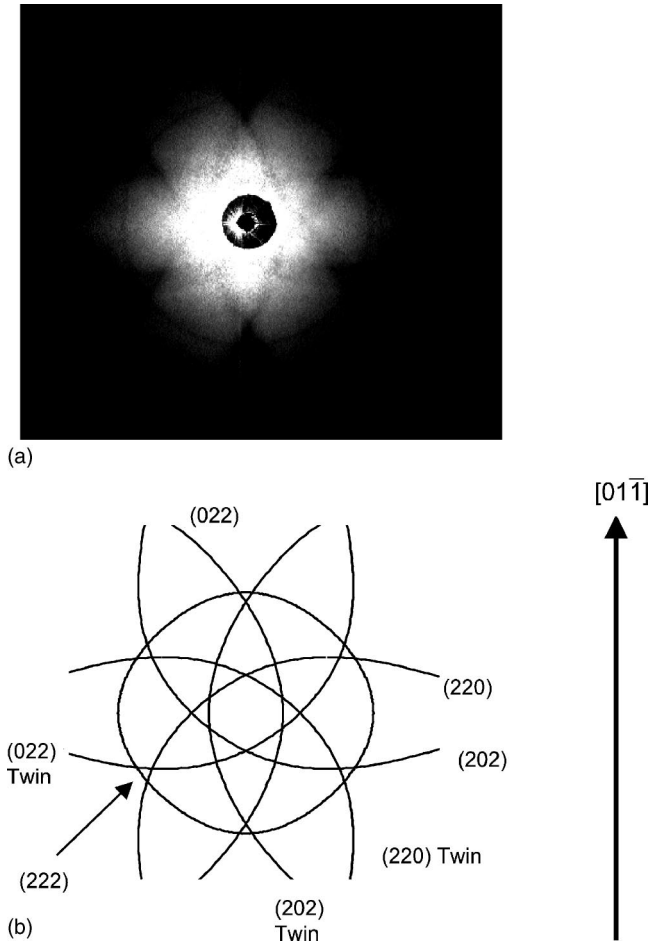

FIG. 5. (a) CCD image of backward scattered Kossel lines from CCA, where 488 nm light illuminated the sample at normal incidence. (b) Kossel ring pattern calculated using measured crystal parameters. The Kossel lines are indexed with the [111] direction normal to the page and the $[01\bar{1}]$ direction vertical. The modeled sixfold symmetry results from fcc crystal twinning.

faults. The apices of the 2D diffraction spot hexagon did not occur along the line connecting the filling holes (Fig. 4). This indicates that the shear forces associated with sample flow orient the fcc (111) planes.

Kossel rings occur when defects within a crystal scatter some of the incident light, to create a diffuse background illumination [19,20,35]. Light scattered at angles meeting the Bragg diffraction condition cannot propagate. The locus of angles where light may not propagate form the surfaces of cones, which when projected onto a flat screen appear as dark circles or ellipses against the diffuse light background [19,20,35]. Each set of diffracting planes gives rise to a set of Kossel rings oriented about an axis normal to the set of planes. The interior angle of the cone is the complement of the Bragg angle θ_b. Different crystal structures and lattice spacings gives rise to different Kossel ring patterns and spacings. These Kossel ring patterns give definitive information on the crystal structure, lattice parameter, and crystal orientation.

Figure 5(a) shows the typical Kossel ring pattern observed with 488 nm light incident normal to the surface of the CCA cell. The central circular ring derives from second-order scattering from the (111) fcc planes. The (111) ring is not visible because it falls outside the imaged area. The other Kossel rings result from the {220} and {311} families of fcc planes. Each of these sets of Kossel rings show sixfold symmetry, rather than the threefold symmetry expected from an fcc structure. The observed sixfold symmetry correlates with the hexagonal symmetry observed for the diffraction of the higher Miller index planes, as discussed above.

The observed Kossel ring pattern is very similar to the calculated Kossel ring pattern shown in Fig. 5(b). This pattern was calculated for a twinned-fcc crystal with the lattice parameter determined from the extinction spectra of Fig. 3. The crystal orientation was specified by assigning the [111] direction to be normal to the cell walls, and the $[01\bar{1}]$ direction to lie along the IR CCA flow direction between filling

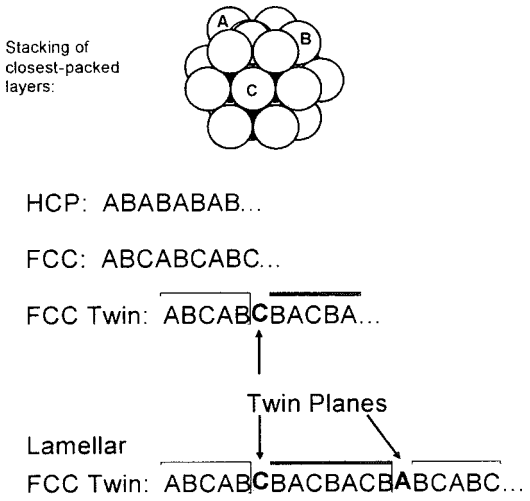

FIG. 6. Stacking of close-pecked layers to form hcp, fcc, or twined-fcc crystals.

ports. The same patterns were observed for all samples. Shear forces have been reported to orient the hexagonally packed surface layers of colloidal crystals [36]. In these CCA the observed pattern is consistent with alignment of the fcc $[0\bar{1}1]$ direction along the shear flow.

The observed hexagonal symmetry probably derives from fcc crystal twinning. In an fcc crystal the closest-packed (111) layers stack in the order *ABCABC*… (Fig. 6). This contrasts with the hcp structure in which the close-packed layers stack *ABAB*… and form the (0001) planes. These layers can stack in other configurations to form a variety of other structures including randomly close-packed structures. One common stacking defect is the twinned fcc crystal, which may be constructed by stacking layers ABCAB *C*BACBA…, where **C** indicates the location of the twin plane boundary. Crystals containing multiple twin planes are known as lamellar twins and have been observed in colloidal crystals using polarized microscopy [37].

We conclude from the 2D and 3D diffraction and the Kossel ring data that the CCA samples are twinned fcc crystals. Stacking faults along the [111] direction create the crystal twins. The alignment of the crystal appears to be determined by the CCA injection shear forces. It is likely that the fluid flows as columns of spheres, which when the flow stops relaxes into hexagonally packed layers. Since crystal growth nucleates at the surface, the fcc crystal probably grows from the walls. Previous studies [37–40] indicated that the formation of twinned crystals is an intermediate step in the growth of colloidal crystals. However, even after sitting undisturbed for as long as one week, we still observe sixfold symmetry of 3D diffraction spots and the sixfold symmetric Kossel ring patterns in these CCA.

B. Diffraction efficiencies

We determined the diffraction efficiencies and bandwidths of these CCA photonic crystals by measurements of the transmission of the incident beam and by measuring the intensity of the diffracted beam. Transmission measurements

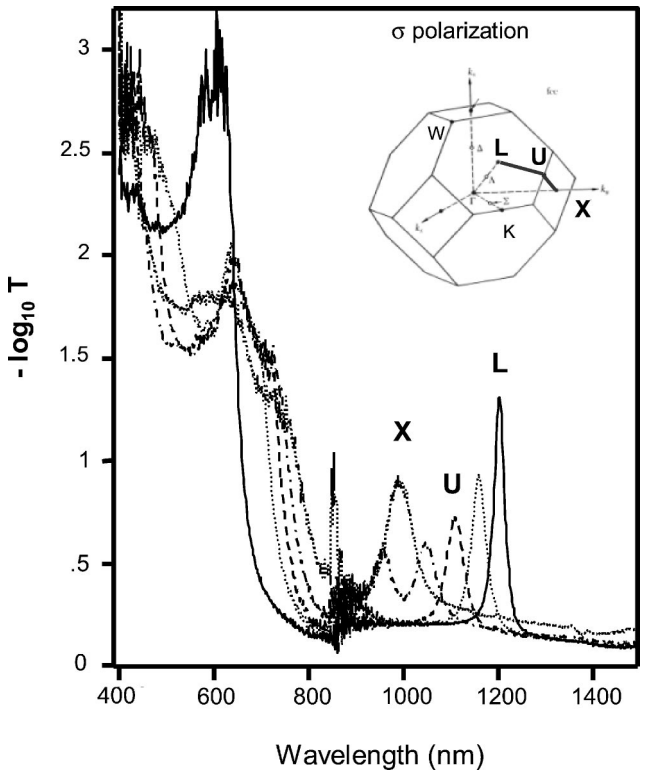

FIG. 7. Transmission spectra of 125 μm thick CCA recorded at different rotation angles within the *L*-*U*-*X* plane. The incident light is polarized perpendicular to the incidence plane. The *L* direction corresponds to normal incidence, *U* is rotated by 35.3°, and *X* is rotated 54.7° from normal. As the CCA is tilted, the (111) diffraction shifts from ~1200 nm to ~1000 nm, where it is coincident with the (200) peak. The broad band at ~600 nm at normal incidence is a superposition of several diffraction peaks from the (200), (220), and (311) families of planes.

monitor the removal of intensity from the forward scattered beam, while diffraction measurements monitor the intensity diffracted by a particular set of planes into a defined solid angle. Most previous reports have focused on transmission measurements. However, as we demonstrated earlier [20], significant light is also diffusely scattered from CCA crystal defects. In addition, the CCA surface layers give rise to significant 2D diffraction.

Figure 7 shows the dependence of transmission as a function of incidence angle for light polarized perpendicular to the plane containing the incident light propagation vector and the diffracting plane normal for a 125 μm thick IR CCA. The sample was oriented with the injection flow direction $[0\bar{1}1]$ along the crystal rotation axis. Rotation of the sample by 54.7° from where the incident beam lies parallel to the [111] direction, to where the incident beam lies parallel to the [200] direction, is equivalent to rotation from *L* to *X* in the fcc Brillouin zone, where *L* corresponds to the [111] direction and *X* corresponds to the [200] direction (Fig. 7). The normal incidence transmission spectra in Fig. 7 shows a sharp narrow peak at ~1200 nm from the (111) planes and a much larger broader peak at ~600 nm, which results from overlapping diffraction from the {200}, {220}, and {311} planes [29], as well as second-order diffraction from the

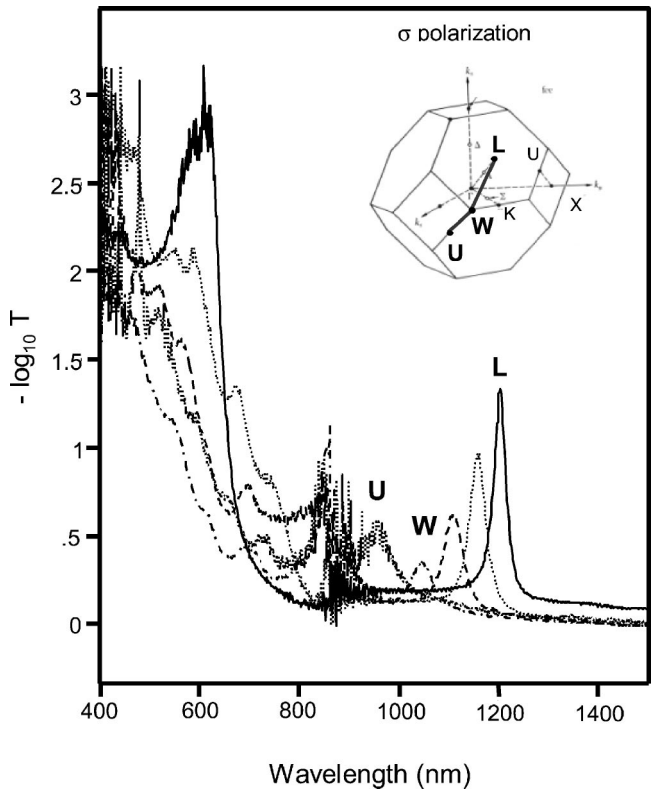

FIG. 8. Transmission spectra from the same 125 nm CCA sample, as in Fig. 7, also with perpendicularly polarized light, but the CCA is rotated in the *L-W-U* plane. The (111) diffraction peak rotates similarly, but diffraction from the higher order planes is weaker, allowing some individual peaks to be resolved.

(111) planes. Diffraction from the higher index planes only overlap when the beam is incident along the [111] direction. Rotating the crystal away from normal incidence removes the overlap [29]. The resulting peaks shift towards longer and shorter wavelengths, which effectively broadens the diffraction to cover the entire visible spectral region.

Rotation of the sample blue shifts the (111) diffraction peak as expected from Bragg's law. We measured transmission as the sample was rotated between *L-W-U* in the Brillouin zone (Fig. 8). This was accomplished by rotating the sample 30° about the [111] direction, followed by rotating the sample in the *L-W-U* plane. There is less extinction in the visible region when the CCA is oriented in this plane because fewer of the high index planes are poised to diffract the incident light. This is in contrast to the rotation within the *L-X* plane, which brings all the higher Miller index diffraction planes into position to diffract. The visible wavelength transmission is decreased compared to that in Fig. 7.

We measured the thickness dependence of the CCA diffraction efficiencies by rotating the crystal such that particular planes met the diffraction condition. We then measured for 488 nm light both the transmitted and diffracted intensity as well as the intensity of the 2D diffraction within the scattering plane. Tables II and III indicate that when the CCA crystal is oriented such that the (111) Bragg diffraction condition is met, the transmission is essentially zero even for the 25 μm thick samples [~56 (111) layers]. Although the

TABLE II. Diffraction and transmittance measurements for fcc (111) plane visible CCA at various particle densities and sample thicknesses.

λ_{111} (90°)	Thickness t (μm)	Specular only		Large aperture		Effective thickness (μm) (Calculated)
		T	D	T	D	
475	40	0.001	0.748	0.002	0.835	
495	40	0.003	0.680	0.006	0.776	
495	125	0.000	0.725	0.000	0.839	
495	250	0.000	0.640	0.000	0.728	
510	40	0.010	0.506	0.052	0.631	5.4
525	40	0.004	0.501	0.041	0.622	5.7
525	125	0.000	0.556	0.001	0.704	
525	250	0.000	0.547	0.000	0.688	
585	40	0.004	0.350	0.054	0.519	5.1
585	125	0.001	0.372	0.003	0.529	5.4
585	250	0.000	0.265	0.001	0.431	4.1
605	40	0.014	0.262	0.079	0.552	4.5
605	125	0.004	0.270	0.010	0.597	4.6
605	250	0.000	0.535	0.001	0.792	10.3

TABLE III. Diffraction intensity measurements for IR CCA samples of various thicknesses for 488 nm incident light.

Sample thickness (μm)	FCC lattice plane	Transmittance	Bragg diffraction efficiency	Total in-plane 2D diffraction efficiency
25	(111)	0.000	0.497	0.020
	2nd(1111)	0.308	0.178	0.034
	(200)	0.135	0.076	0.030
	(220)	0.193	0.38	0.012
	(311)	0.200	0.26	0.017
40	(111)	0.010	0.515	0.022
	2nd(111)	0.000	0.053	0.027
	(200)	0.077	0.045	0.036
	(220)	0.120	0.014	0.026
	(311)	0.099	0.013	0.050
125	(111)	0.000	0.454	0.019
	2nd(111)	0.019	0.034	0.012
	(200)	0.001	0.006	0.013
	(220)	0.000	0.009	0.005
	(311)	0.0000	0.012	0.006
250	(111)	0.000	0.490	0.007
	2nd(111)	0.000	0.088	0.008
	(220)	0.000	0.030	0.000
	(311)	0.000	0.030	0.004

transmission is essentially zero, the total detected intensity of the 2D and 3D diffracted light for the apparently specularly diffracted beam (1.5×10^{-4} sr) is only about half the incident intensity. The diffracted efficiency of the (111) planes is ~50% and is essentially independent of CCA thickness (Table III). Since absorption does not occur, the remainder of the light must be scattered to other angles; significant diffuse diffraction is evident at angles close to the Bragg angle.

The higher index (222), (200), (220), and (311) planes show essentially zero transmission of 488 nm light for the 250 and 125 μm thick CCA. However, the transmission increases to 10–30 % for the 40 μm and 25 μm thickness CCA. We see less than 10% diffraction from these higher order planes. Thus, the higher order planes show even more diffusely scattered intensities. This is visually evident from the diffuse halo around the Bragg diffracted beams.

The different CCA have different particle number densities, which result in different Bragg diffracted wavelengths for normally incident light. λ_{111} is the wavelength of light diffracted by the (111) planes. The sample with λ_{111} =475 nm has a sufficient bandwidth that it also diffracts normally incident 488 nm light. *T* is the fraction of incident light transmitted at the Bragg condition. *D* is the fraction of incident light diffracted by the CCA at the Bragg condition.

We examined the diffractions from CCA which have smaller nearest neighbor spacings (Table II). Since we expect that much of the diffuse scattering will derive from phonon modes, a decrease in the nearest neighbor spacings should result in a deeper potential energy well for each lattice site and smaller rms displacements of particles in the fcc lattice. This should result in an increased diffraction efficiency. This expectation is consistent with the results seen in Table II, which shows the dependence of transmission and diffraction of 488 nm light for CCA samples of different particle densities and sample thicknesses. Negligible transmission occurs for the (111) plane diffraction condition even for 40 μm CCA thicknesses. As observed for the IR CCA, the diffraction efficiencies are significantly below 100%. Although there is some variation with sample thickness, which may be related to changes in defect densities, the efficiency increases monotonically as the nearest neighbor spacing decreases. 75% of the incident intensity is diffracted for the CCA which diffracts 475 nm light at normal incidence. An increase in the detector aperture increases the measured diffraction intensity, indicating that much of the diffusely scattered light is scattered about the Bragg angle.

C. Dynamical diffraction theory (DDT)

Previous attempts to theoretically model diffraction of CCA have mainly utilized dynamical diffraction theory (DDT) [20,41–43]. Assuming a perfect lattice, all of the CCAs discussed here should be in the thick crystal limit of DDT. In this limit all incident light meeting the Bragg condition should be diffracted. Tables II and III clearly show that this is not the case. Since no absorption of light occurs, any light that is not diffracted must be diffusely scattered. Evidence for diffuse scattering includes the increased intensity observed as the detector aperture is increased (Table III).

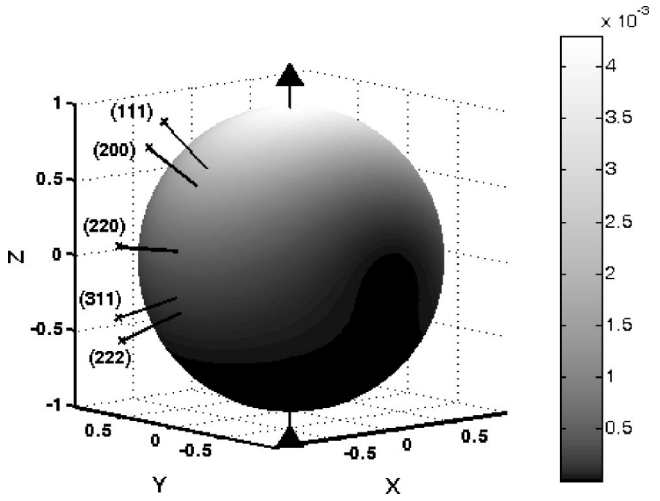

FIG. 9. Spherical surface map shows the efficiency of scattering from crystalline colloidal arrays (CCA). Direction of incident light is indicated by the arrow, while the direction of light scattered by several planes is shown via lines ending with *x*'s. The crystal was rotated about the *z* axis to achieve diffraction by different planes.

This diffuse scattering must arise from phonons or imperfections in the crystal ordering.

The thick crystal limit of DDT is defined by Zachariasen as the regime where $A\gg1$, where *A* is defined as

$$A=\frac{\pi K|\psi_h|n_c t}{\lambda\ \sin(\theta_b)},$$

where *K* is a polarization factor equal to unity when the incident beam is polarized perpendicular to the scattering plane, n_c is the refractive index of the crystal, *t* is the crystal thickness, λ is the incident wavelength in air, θ_b is the Bragg glancing angle, and ψ_h is the Fourier coefficient for the set of diffracting planes. ψ_h can be described as

$$\psi_h=\frac{16\pi\alpha G}{a^3},$$

where *a* is the CCA lattice constant, *G* is a scattering factor, and α is the polarizability of a colloidal sphere [20]:

$$\alpha=\frac{(m^2-1)}{3}r^3.$$

m is the ratio of the particle refractive index to medium (water) refractive index, and n_p/n_w, and *r* is the particle radius. For particles in the Rayleigh-Gans scattering regime [42], *G* is

$$G=\frac{3}{u^3}(\sin u-u\cos u),$$

where *u* is a scattering size parameter:

$$u=\frac{2\pi n_c D_0\sin\theta_b}{\lambda},$$

where D_0 is the particle diameter. n_c is the crystal refractive index

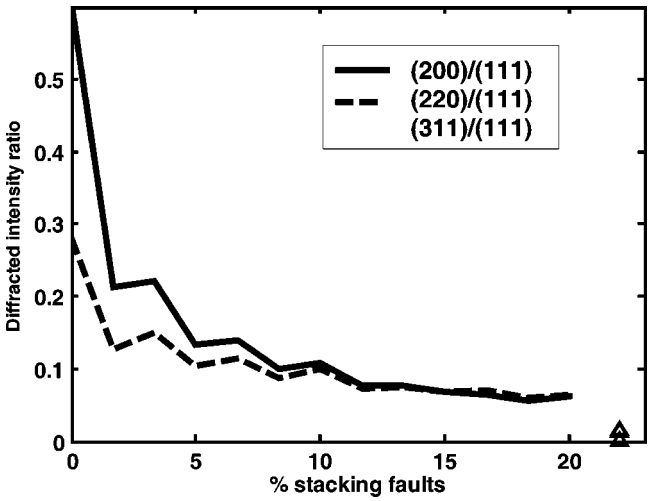

FIG. 10. Dependence of the diffraction intensity from the (200), (220), and (311) planes on the percentage of stacking faults for a CCA containing 60 layers stacked along z with 250×240 particles in each layer. The value plotted is the average intensity ratio relative to the intensity diffracted by the (111) planes. The average values were calculated by averaging the effect of 400 possible configurations of the indicated number of stacking faults. The triangles indicate the diffraction from a random stacked CCA.

$$n_c = n_p\phi + n_w(1-\phi),$$

where n_p and n_w are the refractive indices of polystyrene and water, respectively, and ϕ is the particle volume fraction.

We calculated the effective crystal thicknesses (Table II) by determining the values for A from the DDT expression for Bragg case for diffracted power from a crystal:

$$P_D = \frac{\sin^2[A\sqrt{y^2-1}]}{y^2-1+\sin^2[A\sqrt{y^2-1}]},$$

where y at Bragg condition is related to the angle and crystal parameters by

$$y = \frac{\left(\frac{1-b}{2}\right)\psi_0}{\sqrt{|b|}K|\psi_h|},$$

b is the ratio of direction cosines for the incident and diffracted beams (-1 in this case) and ψ_0 describes the amplitude of the refractive index modulation:

$$\psi_0 = \left(\frac{n_c}{n_w}\right)^2 - 1.$$

As indicated in Table II these equations predict much higher (111) diffraction efficiencies than are observed. For example, for the 525 nm diffracting CCA in Table II we calculate that the diffraction intensity experimentally observed should result from only 30 (111) polystyrene layers in water, a sample thickness of only ~5.7 μm. This clearly indicates that the CCA diffraction efficiency is degraded by CCA disorder. Table III indicates that the diffraction efficiencies from the higher Miller index planes are even smaller than that of the (111) planes, even though the structure factors are identical [19].

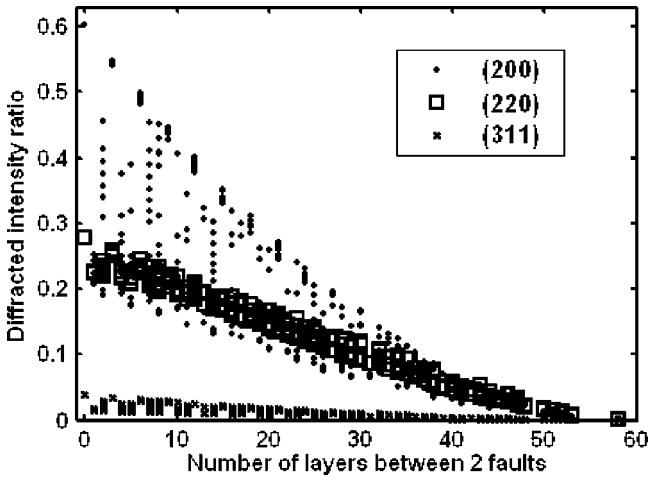

FIG. 11. Diffraction intensity from (200), (220), and (311) planes relative to that from the (111) plane as a function of number of layers between two stacking fault locations. Calculations were performed for two stacking faults which were randomly placed inside 60 (111) layers, and then repeated for 400 different configurations.

The validity of using dynamical diffraction theory to explain the diffraction properties of colloidal crystals was discussed recently by Mittleman *et al.* [43]. These researchers found parallels between dynamical diffraction theory and the scalar wave approximation used to calculate the diffraction properties of photonic crystal materials. They found relatively good agreement between the calculated and measured diffraction bandwidths, but also found that the measured diffraction efficiencies are much lower than predicted.

D. Single particle coherent Mie scattering calculation of diffraction efficiency

Recently, we directly calculated the diffraction efficiencies of CCA in the kinematic limit, where we include the Mie scattering amplitudes of the colloidal particles directly [44]. We calculated the diffraction efficiencies by summing the scattering of each of the individual colloidal spheres together with their corresponding phase factors. Our method, which has some similarity to that of Amos *et al.* [45], will be presented in detail elsewhere.

The difference between our approach and that of Amos *et al.* [45] is that we calculated the integrated diffraction efficiencies for finite crystals. Our calculations indicate (as we will report in a forthcoming paper) that for finite crystals the shape and angular width of the Bragg diffraction peaks differs for diffraction from different crystal planes.

The scattering amplitudes for the individual spheres were calculated exactly from Mie theory [42]. These calculations neglect both the extinction of the incident light propagating through the crystal and multiple scattering. Although these approximations are likely to cause significant errors in the calculation of the absolute diffraction intensities, they are

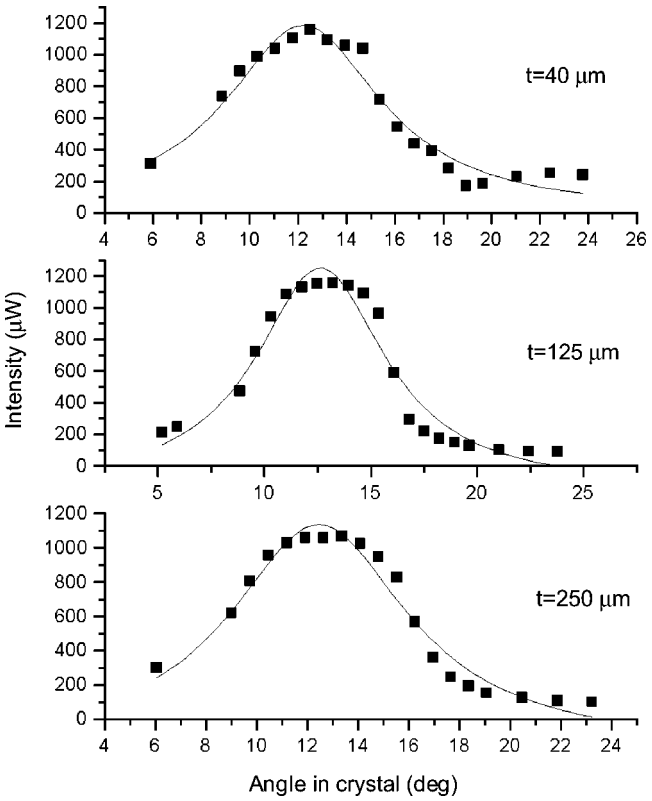

FIG. 12. Diffraction bandwidths of visible CCA that diffracts ~500 nm light at normal incidence. The sample was rotated through the Bragg angle. Intensities were measured by moving the detector along with the rotating sample. Listed bandwidth angles are within the crystal and have been corrected for refraction.

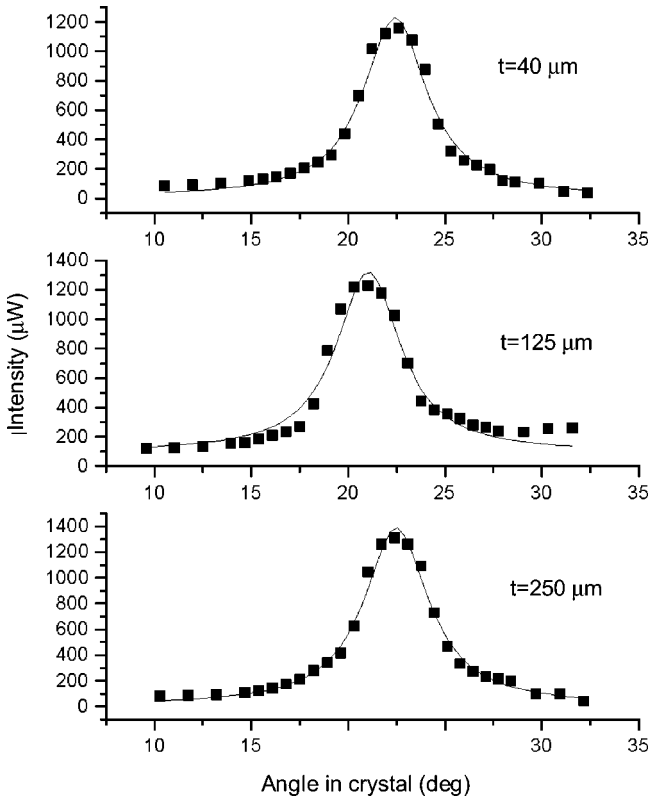

FIG. 13. Diffraction bandwidths from visible CCA that diffracts ~525 nm light at normal incidence. The sample was rotated through the Bragg angle and intensities were measured by rotating the detector along with the sample.

likely to predict well the relative diffraction efficiencies of different Miller index planes. The diffraction of these polystyrene colloids in water actually occurs in the dynamical diffraction limit, which means that extinction is significant.

The diffraction efficiencies of the different Miller index planes for perfect crystals are expected to differ mainly because of the differences in the single sphere scattering factors at the different diffraction angles. We also expect significant alterations in the diffraction of different Miller index planes due to the presence of stacking faults along the normal to the (111) planes.

Figure 9 shows a 3D plot of the calculated CCA scattering intensity for the geometry corresponding to the experimental measurements of Table III. Incident light propagates upward along the *z* direction and is shown by the line ending with an arrow. The diffraction directions from the (111), (200), (220), (311), and (222) planes are shown by lines ending with *x*'s. [the diffraction direction from (222) plane is the same as the second-order diffraction direction from the (111) plane]. Only the azimuthal angle of the diffraction direction is shown in Fig. 9 for simplicity. The crystal requires rotation about the *z* axis to orient each of the planes for diffraction.

The shading of the scattering sphere surface indicates the intensity scattered at each scattering angle. The white at the top pole indicates a strong bias towards forward scattering. Thus, CCA photonic crystals are expected to show a large angular dependence of the diffraction efficiency. This strong angular dependence would not occur for scattering from spheres much smaller than the wavelength of light.

From Mie theory we calculated single sphere diffraction intensity ratios for the diffraction directions from the (111), (222), (200), (220), and (311) planes of 1, 0.02, 0.75, 0.18, and 0.04, respectively. We also calculated the scattering intensities of a CCA consisting of 60 (111) layers stacked along the *z* axis, each of which consists of 250×240 colloidal particles in the *X*,*Y* plane with a lattice spacing, sphere size and refractive index difference identical to that or our experimentally measured IR CCA. For 488 nm incident light onto a perfect crystal we calculated diffraction efficiency ratios for the (111), (222), (200), (220), and (311) planes of 1, 0.01, 0.60, 0.28, and 0.04, respectively. The differences in diffraction efficiencies derive mainly from the differences in the single sphere scattering factors.

We investigated the impact of stacking faults on the diffraction efficiencies from different crystal planes by calculating the average diffraction intensity as a function of the percentage of stacking faults (Fig. 10). A percentage stacking fault of zero corresponds to a perfect fcc crystal. Diffraction intensities from the (111) and (222) planes are, as expected, unaffected by stacking faults. In contrast, the diffraction efficiencies from the (200), (220), and (311) planes dramatically decrease with the number of stacking faults. The impact of a stacking fault depends strongly on its location. For example, a single stacking fault located in the middle of the crystal reduces the diffraction efficiencies by more than two-

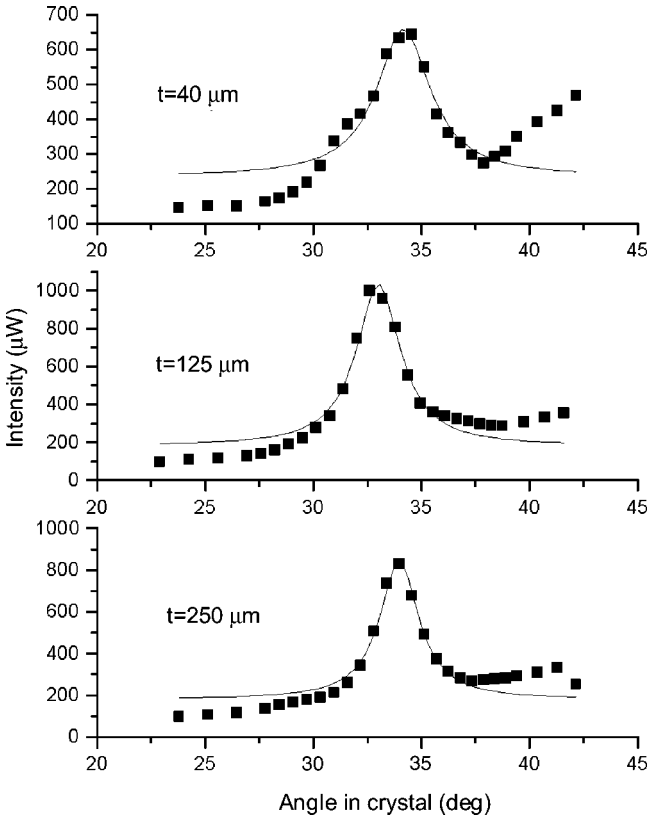

FIG. 14. Diffraction bandwidth measurements of visible CCA that diffracts ~585 nm at normal incidence. The rising background is caused by an increased reflectance from the cell surfaces as the angle of incidence increases. This is most pronounced in the 40 μm sample because it attenuates less light, allowing more contributions from the rear surface reflections.

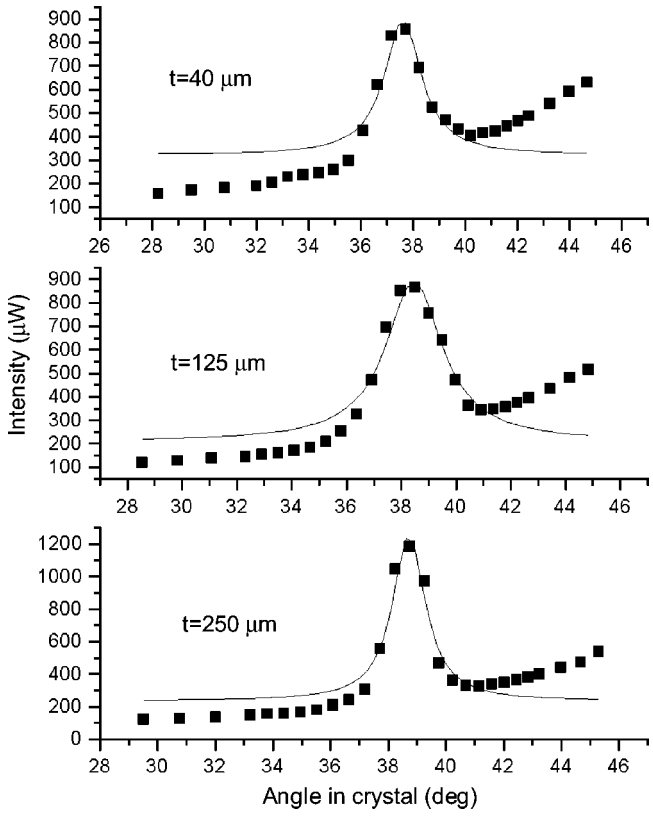

FIG. 15. Diffraction bandwidth measurements for visible CCA that diffracts ~605 nm light at normal incidence. Significant contributions from reflectance create a rising background.

fold. Figure 10 plots the average diffraction intensity calculated from 400 randomly selected stacking fault configurations. In the case of a single stacking fault only 60 configurations are possible. For two faults, 60×59 configurations occur, etc.

These (111) plane stacking faults affect the diffraction of different Miller index planes differently. For example, there is a larger average impact on the diffraction of the (200) plane than on the (220) plane; diffraction from the (200) planes decreases faster as the number of stacking faults increases. For a small number of stacking faults we expect wide variations in the measured intensities of actual crystals due to variations in the stacking fault locations. This is the likely explanation for the significant variation in the relative intensity values diffracted by the (200), (220), and (311) planes as displayed in Table III.

We also calculated the diffraction intensities for a CCA with complete random stacking of the (111) planes. The diffraction ratios for the (111), (200), (220), and (311) planes in a random stacked CCA were calculated to be 1, 0.0131, 0.0165, and 0.0009, respectively. These values are indicated by triangles in Fig. 10. Again, this random stacking does not impact the diffraction efficiencies of the (111) and (222) planes.

The diffracted intensity from these planes crucially depends on the exact location of the stacking faults within the CCA. Figure 11 plots the ratios of diffraction intensities for the (200), (220), and (311) planes relative to the diffracted intensity from the (111) plane for each of 400 possible locations of two randomly placed stacking faults within the 60 (111) layers. As the absicca we use the number of layers (which could be of *A*, *B*, or *C* type) between the two stacking faults. When we have just two stacking faults, our crystal consists of three segments with the middle part between stacking faults of type (*ACB*…), and the outer two parts are of type (*ABC*…). We see that by using the number of layers between stacking faults as a plotting parameter for the *X* axis, we calculate multiple values for the diffracted intensity ratio depending on the site of the stacking faults. This shows that diffracted intensities depend strongly on both the number of layers between the faults and the exact locations of the faults inside the crystal. Two stacking faults within 60 layers correspond to 3.33% of stacking faults. We take the average of all diffracted intensities from the (200), (220), and (311) planes from Fig. 11 to obtain the average value of intensities for 3.33% of stacking faults and plot this single value in Fig. 10.

Stacking fault disorder is probably responsible for most of the losses in diffraction efficiency of the higher Miller index planes. A stacking fault removes particles from the higher order planes which decreases the dielectric constant modulation.

Figure 11 shows that the (200) diffraction intensity ratio maximizes for every three layers added between two stack-

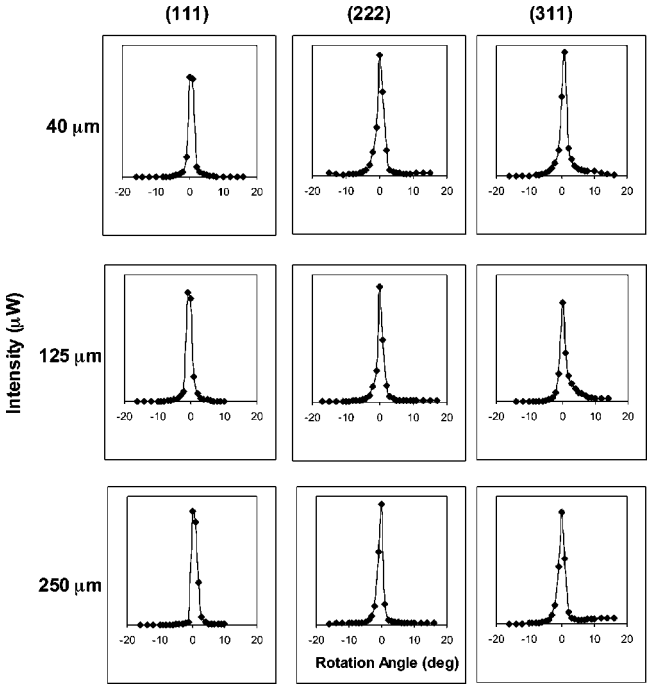

FIG. 16. Angular bandwidth measurements of fcc diffraction for IR CCA. The data shown are the relative intensity as a function of rotation angle away from the maximum diffraction angle for the (111), (222), and (311) sets of planes for different thickness CCA samples.

ing faults. For a perfect fcc crystal, the ratio is 0.6. The ratio decreases to 0.25 when a single layer is introduced between two stacking faults. It varies between 0.2 and 0.45 for two layers and maximizes at 0.55 for three layers and then decreases to 0.26 for four layers. This behavior results from the phase factor introduced by the planes added between two stacking faults.

E. Diffraction bandwidths

We measured the angular diffraction bandwidths (full width at half maximum) for the visible and IR CCA samples by measuring the angular dependence of the intensities of the diffracted beam, rather than by measuring white light transmission spectra. This allows us to directly separate diffraction from attenuation of the incident beam by diffuse scattering. This also permits measurements of diffraction even when different sets of planes diffract the incident light simultaneously.

Figures 12–15 show the results of the angular bandwidth measurements for the visible CCA, while Fig. 16 shows similar measurements for the IR CCA. The angles listed are within the CCA and have been corrected for refraction. The intensities include both the diffracted light and reflections from the cell surfaces. The solid lines are Gaussian fits to the data points. The rising backgrounds in the more dilute samples (Figs. 14 and 15) are caused by increased reflection intensities at the large incident angles. Table IV lists the measured bandwidths from the curve fits along with the bandwidths calculated using dynamical diffraction theory.

TABLE IV. Measured and calculated angular diffraction bandwidths for the visible CCA.

λ_{111}		Angular bandwidth		
(90°)	Thickness (μm)	Measured	Calculated	
			Thick crystal limit	Intermediate crystal limit
500	40	7.9		
	125	7.4	8.40	11.64
	250	8.6		
525	40	4.0		
	125	4.1	4.81	8.00
	250	4.0		
585	40	3.6		
	125	2.6	2.95	7.01
	250	2.3		
605	40	1.9		
	125	2.4	2.68	7.10
	250	1.5		

Dynamical diffraction theory predicts that the angular full width at half maximum value in the thick crystal limit is $w_\theta = |K\psi_h| / \sqrt{b} \sin(2\theta_b)$. We find that the measured angular bandwidths are very close to those predicted in the thick crystal limit (as seen in Table IV), in contrast to the fact that the measured diffraction intensities are much smaller than those expected theoretically, as discussed above. The effective thicknesses determined from the diffraction intensity measurements were used to calculate the angular bandwidths by using the DDT equations for the intermediate crystal thickness regime. The bandwidth in the intermediate thickness limit is

$$w_\theta = \sqrt{\frac{\log_{10} 2}{3\pi}} \frac{4\lambda}{t \sin(2\theta_b)}.$$

As seen in Table IV, bandwidths calculated using this method are larger than those experimentally measured.

Angular bandwidths for diffraction from the (111), (222), and (311) fcc planes of the IR CCA were measured for samples of various thicknesses (Fig. 16, Table V). As indicated in Table V the bandwidths predicted by DDT for the thick crystal case are generally larger than those observed. The bandwidths of the (111) and (311) diffraction spots in-

TABLE V. Calculated and measured diffraction angular bandwidths from IR CCA.

Plane	(111) (deg)	Second (111) (deg)	(311) (deg)
Calculated	5.86	3.32	3.27
40 μm	1.24	1.59	1.62
125 μm	1.52	1.25	1.63
250 μm	1.67	1.22	1.78

crease with sample thickness, but the width of the second-order (111) diffraction decreased. It is surprising that the bandwidth of the (111) and second (111) sets of planes would have opposite trends.

The measured bandwidths were determined from Gaussian curve fits to the angular intensity measurements (Figs. 12–15). Bandwidths from the visible CCA (Table IV) were calculated using dynamical diffraction theory for both the thick crystal limit and for the intermediate crystal limit using the effective thickness values from Table II.

Bandwidths from IR CCA (Table V) were calculated using dynamical diffraction theory in the thick crystal limit, and were measured by fitting Gaussian profiles to the plots of relative intensity seen in Fig. 16.

The diffraction bandwidth should decrease as more planes are sampled by the incoming light. The too large bandwidths calculated for the intermediate thickness case (Table IV) indicates that the actual thickness sampled is much larger than that assumed in that calculation. Hence, this crystal diffracts in the dynamical diffraction thick crystal limit. The Table V IR crystal diffraction show bandwidths that are more than a factor of two narrower than those theoretically calculated. This may result from an increase in defects in the IR CCA over the visible wavelength CCA.

IV. CONCLUSIONS

We have examined the optical diffraction from photonic crystal CCA of 119 nm diameter polystyrene colloid diffracting between 500 and 600 nm, as well as IR CCA of 270 nm polystyrene colloid whose lattice constant is large enough ($\sim$766 nm) to allow observation of diffraction from higher order Miller index planes. The structure of these CCA, which were determined using Kossel ring analysis and through measurements of the diffraction spot angles, was found to be twinned-fcc in all cases. Crystal twins, attributed to stacking faults in the layering of the (111) crystal planes, were seen in all IR CCA samples. The twinning stacking faults occur along the normal to the (111) planes. These stacking faults have little impact on the diffraction efficiency of the (111) planes but dramatically decrease the diffraction efficiency of the higher order Miller indices planes. We measured the optical transmission and diffraction properties of these CCA and found that, although little light is transmitted at a variety of angles, only a fraction of that light is diffracted into a narrow beam.

The direction in which the CCA flowed into the sample chamber was found to orient the crystal along the $[01\bar{1}]$ direction. These structural findings may have use in PBGC fabrication since oriented single crystals can be manufactured by flowing the CCA sample.

We attempted to model the diffraction of these CCA using dynamical diffraction theory and using single-particle coherent Mie scattering theory. The diffraction bandwidths predicted by DDT match the experimental results reasonably well, but the measured diffraction intensities are much lower. We also investigated the stacking fault dependence of the relative diffracted intensities from different crystal planes. The lack of better agreement results mainly from a lack of crystal perfection, evidenced by stacking faults that create the crystal twins. We also observe significant intensities of diffuse scattering which derives from other defects.

ACKNOWLEDGMENTS

We wish to thank Chad Reese and Dr. Guisheng Pan for colloid synthesis and characterization. This work was supported by the Defense Advanced Research Projects Administration (Grant Nos. DAAG 55-98-1-0025 and DAAD 16-99-C-1036), the Office of Naval Research (Grant No. N00014-94-1-0592), NIH Grant Nos. DK55348 and GM58821, and NSF Grant No. EE C008 5480 to R.D.C.

[1] J. D. Joannopoulos, R. D. Meade, and J. N. Winn, *Photonic Crystals: Molding the Flow of Light* (Princeton University Press, Princeton, 1995); M. Ibanescu, Y. Fink, S. Fan, E. L. Thomas, and J. D. Joannopoulos, Science **289**, 415 (2000); M. Maldovan, A. M. Urbas, N. Yufa, W. C. Carter, and E. L. Thomas, Phys. Rev. B **65**, 165123 (2002); C. M. Soukoulis, Nanotechnology **13**, 420 (2002); K. Sakoda, in *Optical Properties of Photonic Crystals*, Springer Series in Optical Sciences Vol. 80 (Springer, New York, 2001).

[2] S. John, Phys. Rev. Lett. **58**, 2486 (1987).

[3] R. Biswas, M. M. Sigalas, G. Subramania, and K. M. Ho, Phys. Rev. B **57**, 3701 (1998); R. Biswas, M. M. Sigalas, G. Subramania, C. M. Soukoulis, and K. M. Ho, *ibid.* **61**, 4549 (2000).

[4] K. M. Ho, C. T. Chan, and C. M. Soukoulis, Phys. Rev. Lett. **65**, 3152 (1990).

[5] K. Busch and S. John, Phys. Rev. E **58**, 3896 (1998).

[6] K. M. Ho, C. T. Chan, C. M. Soukoulis, R. Biswas, and M. Siglas, Solid State Commun. **89**, 413 (1994).

[7] E. Yablonovitch, J. Opt. Soc. Am. B **10**, 283 (1993).

[8] E. Yablonovitch, J. Phys.: Condens. Matter **5**, 2443 (1993).

[9] C. C. Cheng and A. Scherer, J. Vac. Sci. Technol. B **13**, 2696 (1995); T. F. Krauss and R. M. De La Rue, Prog. Quantum Electron. **23**, 51 (1999); G. A. Ozin and S. M. Yang, Adv. Funct. Mater. **11**, 95 (2001); P. Jiang, G. N. Ostojic, R. Narat, D. Mittleman, and V. L. Colvin, Adv. Mat. **13**, 389 (2001); D. J. Norris and Y. A. Vlasov, *ibid.* **13**, 371 (2001).

[10] J. E. G. J. Wijnhover and W. L Vos, Science **281**, 802 (1998).

[11] I. I. Tarhan and G. H. Watson, Phys. Rev. Lett. **76**, 315 (1996).

[12] V. N. Bogomolov, S. V. Goponenko, A. M. Kapitonov, A. V. Prokofiev, A. N. Ponyavina, N. I. Silvanovich, and S. M. Samoilovich, Appl. Phys. A: Mater. Sci. Process. **63**, 613 (1996).

[13] S. Y. Lin, J. G. Fleming, D. L. Hetherington, B. K. Smith, R. Biswas, H. M. Ho, M. M. Sigalas, W. Zubrzycki, S. R. Kurtz, and J. Bur, Nature (London) **394**, 251 (1998).

[14] A. Imhof and D. J. Pine, Nature (London) **389**, 948 (1997).

[15] B. T. Holland, C. F. Blanford, and A. Stein, Nature (London) **281**, 538 (1998).

[16] A. A. Zakhidov, R. H. Baughman, Z. Iqbal, I. Khayrullin, S. O. Dantas, I. Marti, and V. G. Ralchencko, Science **282**, 897 (1998).
[17] I. M. Kreiger and F. M. O'Neill, J. Am. Chem. Soc. **90**, 3114 (1968).
[18] P. A. Hiltner and I. M. Krieger, J. Phys. Chem. **73**, 2729 (1969).
[19] R. J. Carlson and S. A. Asher, Appl. Spectrosc. **38**, 297 (1984).
[20] P. A. Rundquist, P. Photinos, S. Jagannathan, and S. A. Asher, J. Chem. Phys. **91**, 4932 (1989); R. Kesavamoorthy, S. Jagannathan, P. A. Rundquist, and S. A. Asher, *ibid.* **94**, 5172 (1991); P. A. Rundquist, R. Kesavamoorthy, S. Jagannathan, and S. A. Asher, *ibid.* **95**, 1249 (1991).
[21] I. I. Tarhan, M. P. Zinkin, and G. H. Watson, Opt. Lett. **20**, 1571 (1995).
[22] P. L. Flaugh, S. E. O'Donnell, and S. A. Asher, Appl. Spectrosc. **38**, 847 (1984).
[23] S. A. Asher, P. L. Flaugh, and G. Washinger, Spectroscopy (Amsterdam) **1**, 26 (1986).
[24] S. A. Asher and S. Jagannathan, U.S. Patent No. 5,281,370 (1994).
[25] S. A. Asher, U.S. Patents Nos. 4,627,689 and 4,632,517 (1986).
[26] J. M. Weissman, H. B. Sunkara., A. S. Tse, and S. A. Asher, Science **274**, 959 (1996); M. Kamenjicki, I. K. Lednev, A. Mikhonin, R. Kasavamoorthy, Adv. Funct. Mater. (to be published); R. Kesavamoorthy, M. S. Super, and S. A. Asher, J. Appl. Phys. **71**, 1116 (1992); S. A. Asher, R. Kesavamoorthy, S. Jagannathan, and P. Rundquist, in Proceedings of the SPIE, edited by R. A. Fisher and J. F. Reintjes (SPIE, Bellingham, WA, 1992), Vol. 1626, p. 238; G. Pan, R. Kesavamoorthy, and S. A. Asher, Phys. Rev. Lett. **78**, 3860 (1997); G. Pan, A. S. Tse, R. Kesavamoorthy, and S. A. Asher, J. Am. Chem. Soc. **120**, 6518 (1998); G. Pan, R. Kesavamoorthy, and S. A. Asher, *ibid.* **120**, 6525 (1998).
[27] J. H. Holtz and S. A. Asher, Nature (London) **389**, 829 (1997); J. H. Holtz, J. S. W. Holtz, C. H. Munro, and S. A. Asher, Anal. Chem. **70**, 780 (1998).
[28] S. A. Asher, V. L. Alexeev, A. V. Goponenko, A. C. Sharma, I. K. Lednev, C. S. Wilcox, and D. N. Finegold, J. Am. Chem. Soc. **125**, 3322 (2003); K. Lee and S. A. Asher, *ibid.* **122**, 9534 (2000); V. L. Alexeev, A. C. Sharma, A. V. Goponenko, S. Das, I. K. Lednev, C. S. Wilcox, D. N. Finegold, and S. A. Asher, Anal. Chem. **75**, 2316 (2003).
[29] L. Liu, P. Li, and S. A. Asher, J. Am. Chem. Soc. **119**, 2729 (1997).
[30] R. D. Pradhan, J. A. Bloodgood, and G. H. Watson, Phys. Rev. B **55**, 9503 (1997).
[31] S. Fan, P. R. Villeneuve, and J. D. Joannopoulos, J. Appl. Phys. **78**, 1415 (1995).
[32] A. Chutinan and S. Noda, J. Opt. Soc. Am. B **16**, 1398 (1999).
[33] A. Chutinan and S. Noda, J. Opt. Soc. Am. B **16**, 2240 (1999).
[34] C. Reese, C. Guerrero, J. Weissman, K. T. Lee, and S. A. Asher, J. Colloid Interface Sci. **232**, 76 (2000); C. Reese and S. Asher, *ibid.* **248**, 41 (2002).
[35] P. Pieranski, Contemp. Phys. **24**, 25 (1983).
[36] M. Tomita, K. Takano, and T. G. M. van de Ven, J. Colloid Interface Sci. **92**, 367 (1983).
[37] Y. Monovoukas and A. P. Gast, Langmuir **7**, 460 (1991).
[38] R. Kesavamoorthy, S. Tandon, S. Xu, S. Jagannathan, and S. A. Asher, J. Colloid Interface Sci. **153**, 188 (1992); S. Tandon, R. Kesavamoorthy, and S. A. Asher, J. Chem. Phys. **109**, 6490 (1998).
[39] T. Yoshiyama and I. S. Sogami, in *Ordering and Phase Transition in Charged Colloids*, edited by A. K. Arora and B. V. R. Tata (VCH, New York, 1996).
[40] H. Versmold, S. Musa, and Ch. Dux, Langmuir **15**, 5065 (1999).
[41] W. H. Zachariasen, *Theory of X-Ray Diffraction in Crystals* (Dover, New York, 1945).
[42] H. C. van de Hulst, *Light Scattering by Small Particles* (Dover, New York, 1957); C. F. Bohren and D. R. Huffman, *Absorption and Scattering of Light by Small Particles* (Wiley, New York, NY, 1983).
[43] D. M. Mittleman, J. F. Bertone, P. Jiang, K. S. Hwang, and V. L. Colvin, J. Chem. Phys. **111**, 345 (1999).
[44] A. Tikhonov, R. D. Coalson, and S. A. Asher (unpublished).
[45] R. M. Amos, J. G. Rarity, P. R. Tapste, T. J. Shepherd, and S. C. Kitson, Phys. Rev. E **61**, 2929 (2000).